PHOTOCATALYTIC GENERATION OF HYDROGEN USING TITANIUM AND BISMUTH OXIDE CATALYSTS

J. O. Peralta-Cruz[1], M. L. Hernández-Pichardo[1*], P. del Angel-Vicente[2]

[1] Instituto Politécnico Nacional, ESIQIE, Laboratorio de nanomateriales sustentables; Av. IPN S/N Col. Zacatenco, 07738, México City, México.

[2] Instituto Mexicano del Petróleo, Dirección de Investigación y Posgrado, Eje Central L. Cárdenas 152, 07730 México City, México.

mhernandezp@ipn.mx

Abstract

Bismuth-based photocatalysts were prepared by a hydrothermal method. The binary $Bi_2Ti_2O_7/Bi_4Ti_3O_{12}$ nanocomposite was obtained by the coupling of both semiconductors. The heterojunction allows an efficient hydrogen generation under UV irradiation, which is superior to the TiO_2 and the Bi_2O_3 oxides. The interfaces observed by HRTEM are possibly in favor of the photoinduced-carriers transport between both semiconductors, assisting the separation of photogenerated electrons and holes. The enhanced photocatalytic hydrogen evolution activity was attributed to an increase of light absorption to generate more photoelectrons and an improved separation of photoinduced electrons and holes, which arises from the internal electric field formed by the heterojunction between $Bi_2Ti_2O_7$ and $Bi_4Ti_3O_{12}$.

Keywords: Hydrogen, photocatalysis, titanium oxide, bismuth oxide, $Bi_2Ti_2O_7/Bi_4Ti_3O_{12}$ nanocomposite.

1. Introduction

The United Nations estimates that the world population will increase by almost 2 billion in the next 30 years. Due to this increase in population and the economic growth associated, it is projected that global energy consumption will increase 2-fold by the midcentury [1]. These human activities will inevitably impact the environment without counting the imminent depletion of fossil fuels. Thus, the serious problem of environmental pollution coupled with the current energy crisis makes the development of clean and renewable energy sources a priority [2].

Therefore, one of the main global challenges is to find a sustainable energy source. Hydrogen, as a carbon-neutral energy carrier, is considered an environmentally friendly and regenerative energy vector [3]. However, most of the hydrogen presently generated is not coming from a clean energy source; the most common is gray or black hydrogen which is neither environmentally friendly nor economical [4, 5]. On the other hand, green hydrogen is produced from a clean source and is a more sustainable alternative. In this sense, solar energy is the most promising exploitable resource since it can provide the energy needed by humans in a year, just in one hour [1]. Thus, hydrogen production from water and solar energy by using a semiconductor is a promising idea that has attracted increasing attention [6, 7]. Photocatalytic production of hydrogen is one of the most promising ways, and the key part of this process is the development of active photocatalysts toward H_2 or O_2 evolution reactions under visible light.

Titanium dioxide (TiO_2) is one of the most widely used semiconductors in photocatalytic processes due to its ability to decompose pollutants into non-toxic substances related to its potential for the formation of photogenerated electrons and holes [8]. Nevertheless, the main drawbacks are wide band gap energy, high recombination of electron-hole pairs generated from visible light, as well as its low quantum efficiency [9]. Then, many efforts have been devoted to improving its efficacy. In this sense, TiO_2 nanostructures to increase the effective photocatalytic surface through the formation of Schottky junctions or heterojunctions have recently been developed [3].

In this regard, bismuth-based photocatalysts are good options for visible-light-driven catalysts [10 – 16]. Among them, bismuth titanates such as $Bi_2Ti_2O_7$ and $Bi_4Ti_3O_{12}$ are part of a large Bi–Ti–O family that have been shown to be effective UV-vis-light photocatalysts [12]. Both materials present a layered

perovskite structure and exhibit good photocatalytic activity due to their adequate bandgap energy and high electron-hole pair separation efficiency. $Bi_2Ti_2O_7$ possesses a bandgap energy of around 2.8 eV [14], which makes it suitable for the photocatalytic splitting of water and degradation of organic contaminants under ultraviolet light irradiation. Meanwhile, $Bi_4Ti_3O_{12}$, on the other hand, has a lower bandgap energy of around 2.9 eV [17], which allows it to respond to visible light in addition to ultraviolet light. It has been used for a variety of photocatalytic applications, including pollutant degradation, water splitting, and CO_2 reduction. Recent studies have shown that combining $Bi_2Ti_2O_7$ and $Bi_4Ti_3O_{12}$ can further enhance their photocatalytic performance, leading to better hydrogen evolution [18]. In this work, we describe the preparation of bismuth-based photocatalysts through and hydrothermal method. The $Bi_2Ti_2O_7/Bi_4Ti_3O_{12}$ heterojunction increased the generation of hydrogen through the improvement of charge separation of photogenerated charge carriers.

2. Experimental Methodology

2.1. *Photocatalysts Preparation*

2.1.1. *Synthesis of the Bi_2O_3 by the hydrothermal method*

The preparation of the bismuth oxides photocatalyst was done by using bismuth (III) chloride ($BiCl_3$, analytical grade, 98 %) as the precursor, which is dispersed in an aqueous sodium hydroxide solution (1.5 M). Then the hydrothermal process was carried out, transferring the solution to a 100 mL Teflon-lined stainless-steel autoclave at a constant temperature of 220 °C for 18 h. Once the hydrothermal process is complete, the autoclave is allowed to cool down to a temperature of 20 °C. The precipitate is collected by centrifugation for 20 min to separate the product formed. The product was washed with distilled water and finally dried at 100 °C for 6 h.

2.1.2. *Synthesis of the $Bi_2Ti_2O_7/Bi_4Ti_3O_{12}$ nanocomposite*

$Bi_2Ti_2O_7/Bi_4Ti_3O_{12}$ nanocomposite was prepared using bismuth (III) chloride ($BiCl_3$, analytical grade, 98 %) and titanium (IV) oxide (TiO_2, analytical grade, nanopowder, 21 nm primary particle size (TEM), ≥99.5 %) both dispersed in a caustic soda solution (1.5 M). The solution is transferred to a 100 mL Teflon-lined

stainless-steel autoclave and maintained at a constant temperature of 220 °C for a period of 18 h. Once the reaction is complete, the autoclave is allowed to cool to room temperature naturally. The precipitate is collected by centrifugation for 20 minutes at 7000 rpm to separate the product formed. The product was washed with distilled water and finally dried at 100 °C for 6 h. This sample was identified as BT2/BT4.

2.2. *Samples characterization*

The samples were characterized by X-ray diffraction by using a RIGAKU Miniflex 600 diffractometer with an X-ray tube with CuKα radiation (λ=1.5418 Å) with linear focus. The power used is 40 kV and 15 mA. An area Dtex high-speed detector is used to obtain high-quality diffraction patterns in less time. The step size is 0.02, and the speed is 5 °/min.

To carry out the X-ray photoelectric spectroscopy (XPS) analysis, a Thermo Scientific K-Alpha equipment with an AlK α source and a monochromator was used. The general spectra are obtained using a step energy of 160 eV and 60 eV for the high-resolution spectra using a load compensation system. Raman spectroscopy analyses were carried out using a HORIBA, Jobin Yvon spectrometer equipped with a CCD detector using a helium-neon laser (wavelength 633 nm). The UV-vis spectroscopy analysis was performed using a Perkin Elmer Lambda 365 UV-Vis equipment at 200-800 nm wavelength.

Finally, the samples were studied by high-resolution transmission electron microscopy (HRTEM), and the micrographs were obtained in a TITAN 80-300 with Schottky-type field emission gun operating at 300 kV. The point resolution and the information limit were better than 0.085 nm. HRTEM digital images were obtained using a CCD camera and Digital Micrograph Software from GATAN. In order to prepare the materials for observation, the powder samples were ultrasonically dispersed in ethanol and supported on holey carbon-coated copper grids.

2.3. *Photocatalytic Test for hydrogen production*

The photocatalytic behavior of the samples for the generation of H_2 was carried out using a water/methanol solution under UV irradiation. In a typical experiment, 0.01 g of the photocatalyst is dispersed in 150 mL of the water/methanol (1:1 volume) solution. The reactor is closed and irradiated with a Pen

Ray Hg UV lamp (254 nm, 4.4 mW/cm^2). The products were identified using a Perkin-Elmer model Clarus 480 chromatograph.

3. Results and discussion

3.1. *Physicochemical characterization of the samples*

Samples of bismuth oxide (Bi_2O_3) and the hybrid nanocomposite $Bi_2Ti_2O_7$/ $Bi_4Ti_3O_{12}$ (BT2/BT4) were synthesized. The results were compared with commercial TiO_2. Figure 1 shows the diffraction patterns of the pure oxides of TiO_2 and Bi_2O_3. In the TiO_2 sample (Figure 1a), the diffraction peaks are identified as the anatase and rutile phases [19], while for the Bi_2O_3 sample (Figure 1b), the peaks were identified as the monoclinic (α- Bi_2O_3) and tetragonal (β- Bi_2O_3) phases [20].
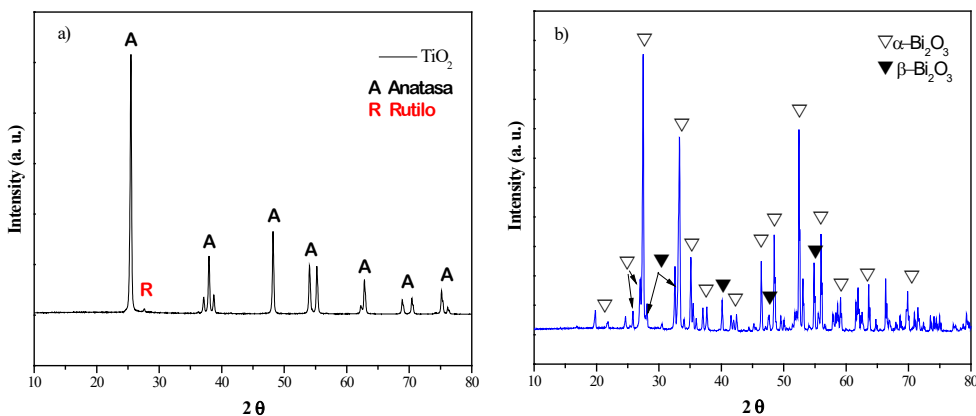

Figure 1. Diffraction patterns for the pristine oxides: a) TiO_2 and b) Bi_2O_3.

Also, Figure 2 shows the diffraction patterns of the three samples of TiO_2, Bi_2O_3, and BT2/BT4 in order to show the formation of the new bismuth titanate phases clearly. In the BT2/BT4 sample, the peaks corresponding to the cubic phases of $Bi_2Ti_2O_7$ (JCPDS-32-0118) and orthorhombic perovskite of $Bi_4Ti_3O_{12}$ (JCPDS-35-0795) [21] appear. The simultaneous presence of all the diffraction peaks of the $Bi_2Ti_2O_7$/$Bi_4Ti_3O_{12}$ phases in the BT2/BT4 sample indicates the formation of the nanocomposite. The fraction of the $Bi_4Ti_3O_{12}$ phase in BT2/BT4 was estimated using the Match ® program, and it was found that 56.9 % corresponds to $Bi_4Ti_3O_{12}$, while 43.1 % was assigned to the formation of $Bi_2Ti_2O_7$.
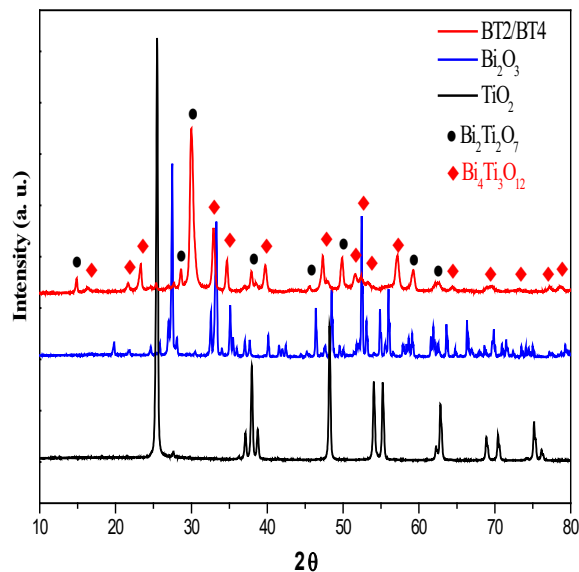
Figure 2. Comparison of the diffraction patterns of the individual oxides with the nanocomposite formed $Bi_2Ti_2O_7/Bi_4Ti_3O_{12}$ (BT2/BT4).

The surface composition and analysis of the chemical states of the BT2/BT4 hybrid composite were analyzed by XPS (Figure 3). Figure 3a shows the survey spectrum of the BT2/BT4 sample in which the peaks of the elements Bi, Ti, and O are observed. Likewise, the high-resolution spectra in the Bi 4f, Ti 2p, Bi 4d regions, and O 1s are shown in Figures 3b to 3d.

The high-resolution spectrum in the Bi 4f region is shown in Figure 3b. The presence of two peaks at 163.9 and 158.6 eV corresponding to the Bi $4f_{5/2}$ and $4f_{7/2}$ signals, respectively, indicating the presence of Bi^{3+} [20], is observed. In Figure 3c, the maximum signal of Ti $2p_{3/2}$ is observed at 457.5 eV, while the maximum signal of Ti $2p_{1/2}$ at 463.6 eV is partially covered by the maximum signal of Bi $4d_{3/2}$ at 465.7 eV, which leads to an overall maximum signal at about 465.5 eV. As shown in Figure 3d, the maximum signals at 529.26 eV and 531.08 eV are assigned to lattice oxygen and adsorbed oxygen. Therefore, with the previous results, there is evidence of the formation and presence of bismuth titanate on the catalyst surface.

Raman spectroscopy was used to verify the structure of the nanomaterials. Figure 4 shows the Raman spectrum of Bi_2O_3 between 100 and 700 cm^{-1} . It is observed that the spectrum presents many signals because α-Bi_2O_3 is a double
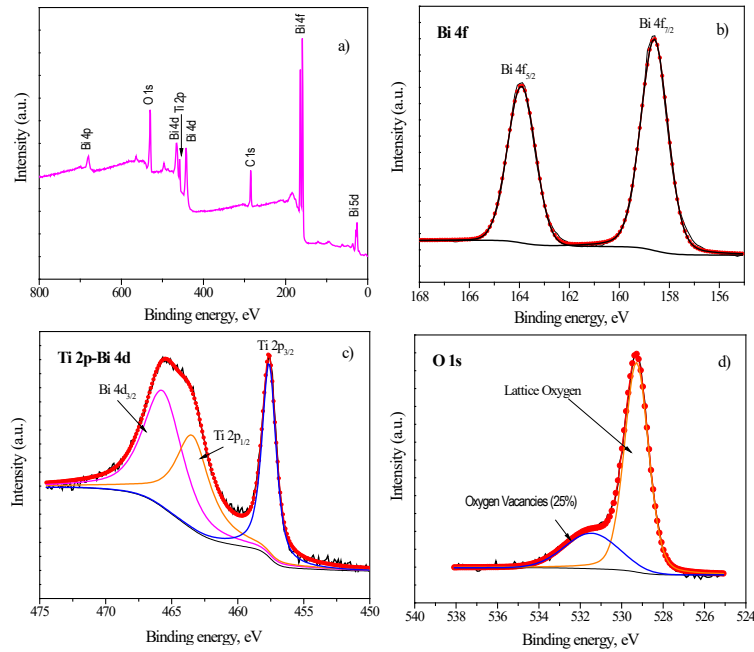
Figure 3. XPS spectra of the BT2/BT4 composite: a) Survey spectrum, b) Bi 4f region,
c) Ti 2p-Bi 4d region, and d) O 1s region.

refraction biaxial crystal with a lower symmetry of the monoclinic structure. Ten typical Bi_2O_3 Raman peaks are observed above 100 cm^{-1} [22], confirming the formation of monoclinic α-Bi_2O_3. The mode at 119 cm^{-1} comes from the Ag symmetry caused mainly by the participation of Bi atoms. The 138 (Ag) and 153 cm^{-1} (Bg) modes can come from the displacements of the Bi and O atoms in the α-Bi_2O_3 lattice.
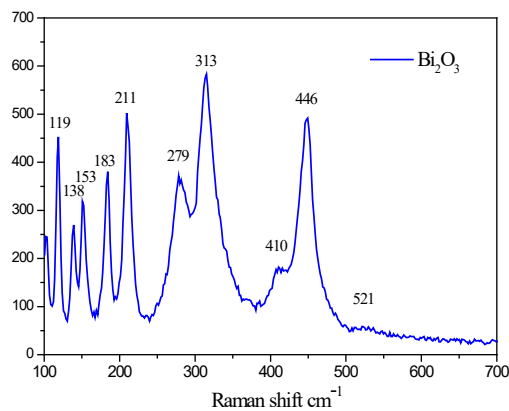

Figure 4. Raman spectra of Bi_2O_3 in the range of 100 to 700 cm-1.

On the other hand, Figure 5 shows the Raman spectrum of TiO_2 between 100 and 700 cm^{-1}. Four characteristic Raman active modes of anatase TiO_2 were observed with symmetries Eg, B1g, A1g, and Eg at 142, 394, 515, and 639 cm^{-1}, respectively, corresponding to the anatase TiO_2 phase [23]. No peaks corresponding to the formation of traces of rutile were observed due to the low amount of this phase in the material.
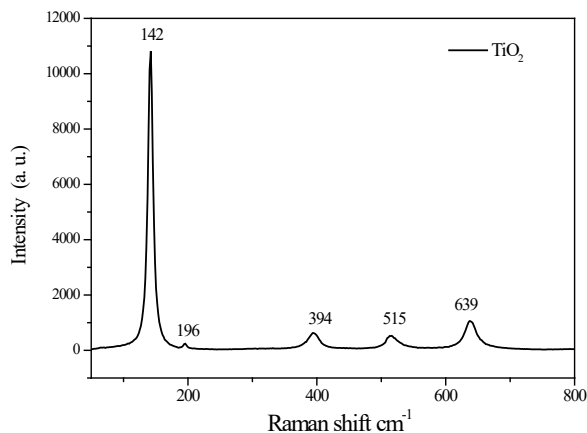

Figure 5. Raman spectra of TiO_2 in the range from 100 to 700 cm^{-1}.

Finally, Figure 6 shows the Raman spectrum of the BT2/BT4 composite between 100 and 1000 cm^{-1}. The spectrum exhibits signals at approximately 117, 142, 229, 271, 323, 537, 566, 617, and 850 cm^{-1}, which are attributed to the internal vibrational modes of $Bi_4Ti_3O_{12}$ [23]. The signals corresponding to $Bi_2Ti_2O_7$ were not observed since they overlap with the other titanate, $Bi_2Ti_2O_{12}$ [24].
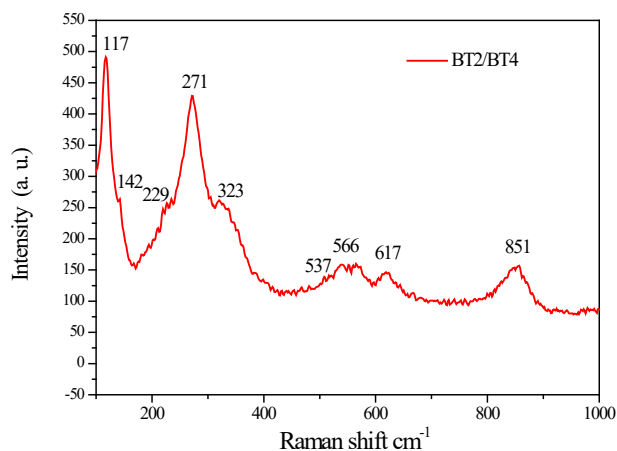

Figure 6. Raman spectra of composite BT2/BT4 in the range of 100 to 900 cm-1.

On the other hand, Figures 7a and 8a show the UV-vis absorption spectra of Bi_2O_3 and the BT2/BT4 composite, respectively, in the wavelength range of 200 to 800 nm in which deionized water has been used as a reference solvent. The optical bandgap has been calculated using the formula of the Tauc method, which relates the optical bandgap (Eg) to the absorption coefficient F(R) and the photon energy (hν) with respect to the relationship $(F(R)*hν)^n \propto (hν-Eg)$, where n is associated with the different types of electronic transitions, in which it can take values of 1/2 or 2 for direct and indirect transitions respectively [25]. Here we have calculated the optical band gap considering the direct transition allowed (n=1/2) because it presents the best fit to the data.

Figures 7b and 8b show a plot between F(R)*hν and the photon energy of bismuth oxide (Bi_2O_3) and the BT2/BT4 composite, respectively. The optical bandgap energy has been determined by extrapolating the linear portion of $[F(R)*hν]^{1/2}$ vs. hν to the x-axis (see Figures 7b and 8b). The Bi_2O_3 bandgap value
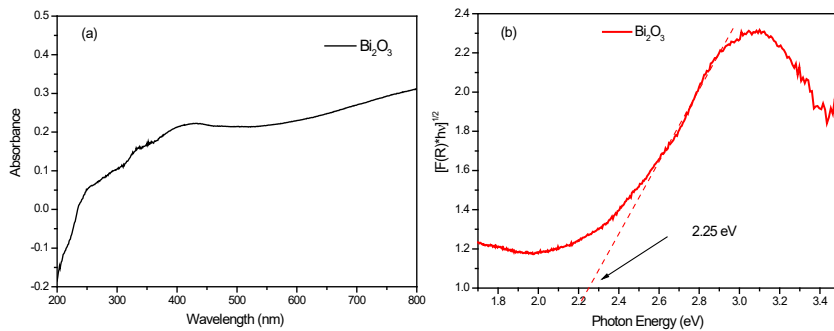

Figure 7. a) UV-vis spectra of Bi_2O_3 in the range 200 to 800 nm. b) Graph of the Tauc method for determining the optical band gap of Bi_2O_3.
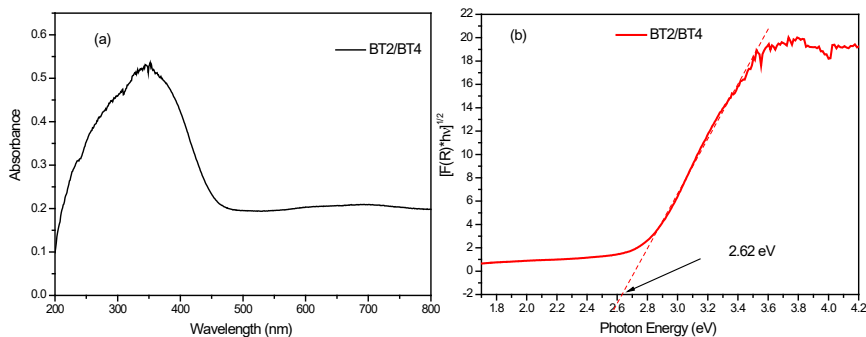

Figure 8. a) UV-vis spectra of the BT2/BT4 composite in the range 200 to 800 nm. b) Graph of the Tauc method for the determination of the optical band gap of the BT2/BT4 composite.

has been found to be 2.25 eV, while the BT2/BT4 composite shows a slightly narrower bandgap than the Bi_2O_3 nanoparticles, with a value of 2.62 eV; these values are close to the bandgap values previously reported [21, 22, 26, 27].

Finally, transmission electron microscopy indicates that the sample presents large crystals of more than 100 nm, which are in contact with nanocrystals of different sizes and shapes smaller than 30 nm, as observed in Figure 9.
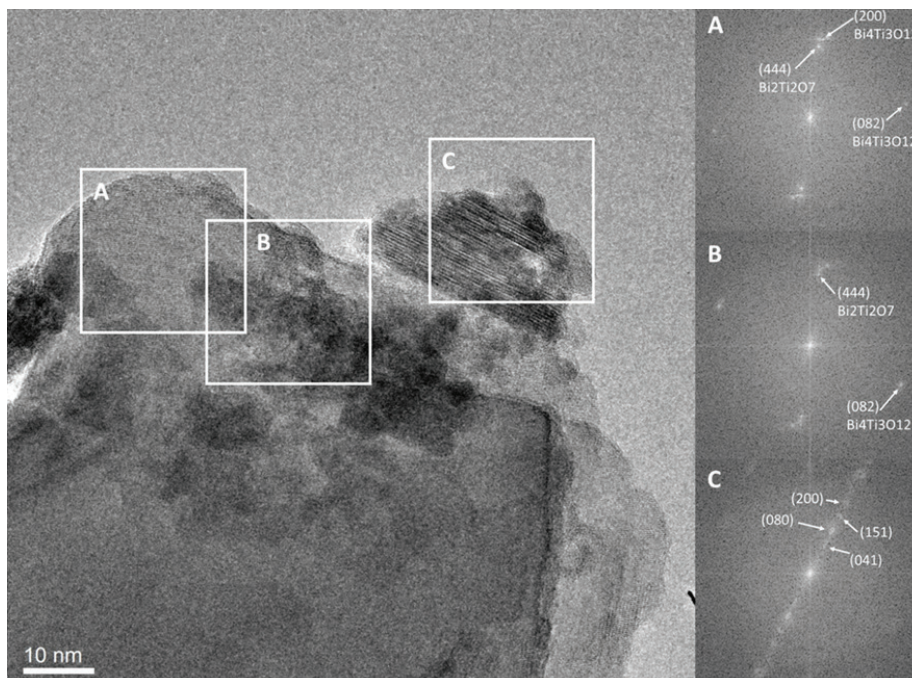

Figure 9. HRTEM image of the BT2/BT4 sample and its corresponding FFT in three zones. A) The FFT indicates that there are two phases, $Bi_2Ti_2O_7$ and $Bi_4Ti_3O_{12}$, B) The same phases were identified as $Bi_2Ti_2O_7$ and $Bi_4Ti_3O_{12}$, C) This crystal was identified as $Bi_4Ti_3O_{12}$; it is an "irregular laminar" crystal that contains planes from 5.5 Å down to less than 2 Å.

The large crystals correspond to the $Bi_2Ti_2O_7$ phase, while nanocrystals generally correspond to $Bi_4Ti_3O_{12}$. In the image, three zones were chosen, and the fast Fourier transform (FFT) of each of them was obtained. In regions A and B, the presence of both phases, $Bi_2Ti_2O_7$ and $Bi_4Ti_3O_{12}$, were identified, while in region C it was possible to analyze a single crystal with atomic planes that correspond to the $Bi_4Ti_3O_{12}$ phase. Here planes of 5.5 Å and 4.5 Å are observed, mainly observing a laminar formation. These interfaces observed by HRTEM are possibly in favor of the photoinduced-carriers transport between both semiconductors, assisting the separation of photogenerated electrons and holes.

3.2. *Photocatalytic performance of bismuth and titanium oxides for hydrogen production*

The photocatalytic performance of the TiO_2, Bi_2O_3, and BT2/BT4 composite for hydrogen production was evaluated under ultraviolet light. The obtained results are shown in Figure 10. The photocatalytic activity of these samples represents the study of four cycles, each cycle corresponding to a determined time of 1 hour, in which the photocatalytic activity of titanium oxide has been used as a reference. The results show that titanium oxide presents the lowest photocatalytic activity; despite this, it presents a constant hydrogen generation during the 4 hours. Bismuth oxide presents a better photocatalytic activity than titanium oxide; the drawback is that it presents a non-constant generation in the second cycle and stabilizes after this. Finally, the BT2/BT4 composite is the one with the highest photocatalytic performance in hydrogen generation, remaining constant during the 4 hours. This enhanced photocatalytic hydrogen evolution activity was attributed to an increase of light absorption to generate more photoelectrons and an improved separation of photoinduced electrons and holes, which arises from the internal electric field formed between the heterojunction between $Bi_2Ti_2O_7$ and $Bi_4Ti_3O_{12}$.
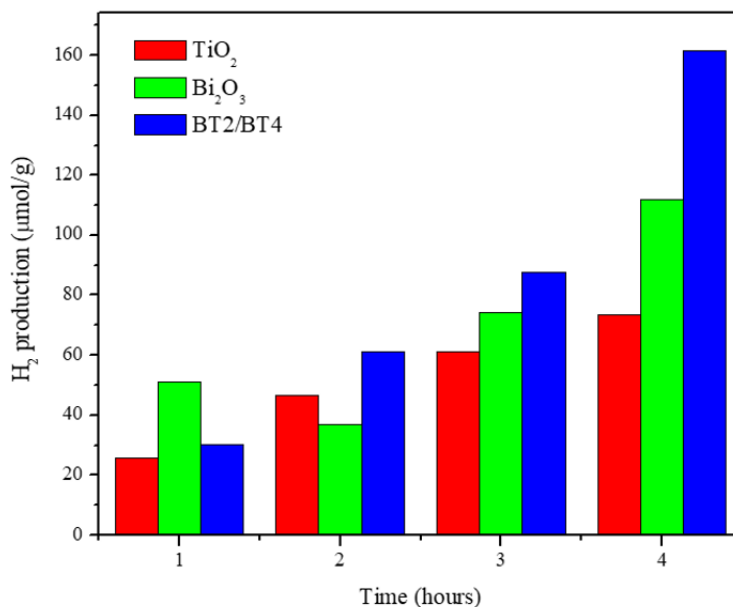

Figure 10. Hydrogen evolution amounts under UV irradiation for TiO2, Bi_2O_3, and the BT2/BT4 composite.

A possible route diagram of the $Bi_2Ti_2O_7/Bi_4Ti_3O_{12}$ composite for hydrogen evolution is shown in Figure 11. The conduction band (CB) and valence band (VB) potential of $Bi_4Ti_3O_{12}$ is more negative than that of $Bi_2Ti_2O_7$ [18]. When the composite is irradiated, producing photogenerated electrons and holes, the electrons in the CB of $Bi_4Ti_3O_{12}$ flow into the CB of $Bi_2Ti_2O_7$ due to closely contacted interfaces. The electric field formed by the heterojunction between $Bi_2Ti_2O_7$ and $Bi_4Ti_3O_{12}$ motivates the separation of the photogenerated electron-hole in both semiconductors. The hydrogen ions accept electrons and convert to hydrogen.
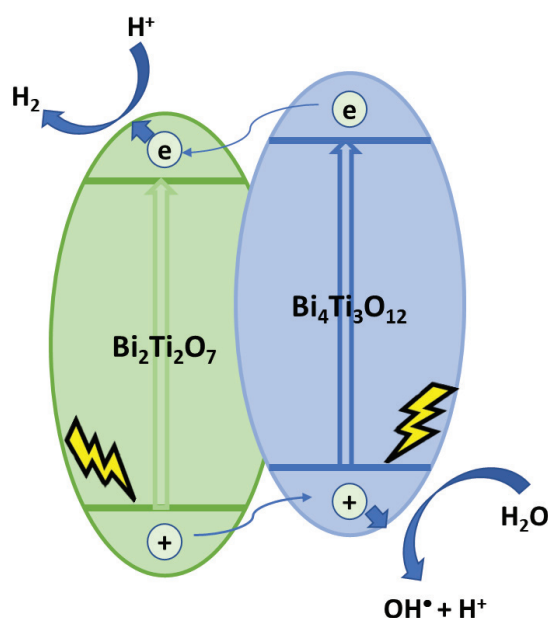

Figure 11. A possible route for the hydrogen evolution for the
BT2/BT4 composite.

4. Conclusions

A $Bi_2Ti_2O_7/Bi_4Ti_3O_{12}$ composite was successfully obtained by a hydrothermal method. The composite is formed by the heterojunction of both phases in intimate contact, as XRD, Raman, XPS, and HRTEM showed. This enhanced photocatalytic hydrogen evolution activity was attributed to an increase of light absorption to generate more photoelectrons and an improved separation of photoinduced electrons and holes, which arises from the internal electric field formed by the heterojunction between $Bi_2Ti_2O_7$ and $Bi_4Ti_3O_{12}$.

Acknowledgment

Funding

References

1. Lewis, N. S., & Nocera, D. G. (2006). Powering the planet: Chemical challenges in so-
    lar energy utilization. *Proceedings of the National Academy of Sciences of the United States of
    America*, 103(43),15729-15735.
    https://doi.org/10.1073/pnas.0603395103

2. Tian, J., Leng, Y., Zhao, Z., Xia, Y., Sang, Y., Hao, P. *et al.* (2015). Carbon quantum dots/
    hydrogenated TiO_2 nanobelt heterostructures and their broad spectrum photocatalytic
    properties under UV, visible, and near-infrared irradiation. *Nano Energy*, 11, 419-427.
    https://doi.org/10.1016/j.nanoen.2014.10.025

3. Cai, J., Huang, J., Ge, M., & Lai, Y. (2018). Multidimensional TiO_2 nanostructured
    catalysts for sustainable H2 generation. *Multifunctional Photocatalytic Materials for Energy*,
    237-288.
    https://doi.org/10.1016/B978-0-08-101977-1.00012-0

4. Aditiya, H. B., & Aziz, M. (2021). Prospect of hydrogen energy in Asia-Pacific: A per-
    spective review on techno-socio-economy nexus. *International Journal of Hydrogen Energy*,
    46(71), 35027-35056.
    https://doi.org/10.1016/B978-0-08-101977-1.00012-0

5. Tarhan, C., & Çil, M. A. (2021). A study on hydrogen, the clean energy of the future:
    Hydrogen storage methods. *Journal of Energy Storage*, 40, 102676.
    https://doi.org/10.1016/j.est.2021.102676

6. Liu, G., Sheng, Y., Ager, J. W., Kraft, M., & Xu, R. (2019). Research advances towards
    large-scale solar hydrogen production from water. *EnergyChem*, 1(2), 100014.
    https://doi.org/10.1016/j.enchem.2019.100014

7. Guo, L., Chen, Y., Su, J., Liu, M., & Liu, Y. (2019). Obstacles of solar-powered photo-
    catalytic water splitting for hydrogen production: A perspective from energy flow and
    mass flow. *Energy*, 172, 1079-1086.
    https://doi.org/10.1016/j.enchem.2019.100014

8. Nakata, K., & Fujishima, A. (2012). TiO_2 photocatalysis: Design and applications. *Journal
    of Photochemistry and Photobiology C: Photochemistry Reviews*, 13(3), 169-189.
    https://doi.org/10.1016/j.jphotochemrev.2012.06.001

9. Koe, W. S., Lee, J. W., Chong, W. C., Pang, Y. L., & Sim, L. C. (2020). An overview of
    photocatalytic degradation: photocatalysts, mechanisms, and development of photocat-
    alytic membrane. *Environmental Science and Pollution Research*, 27, 2522-2565.
    https://doi.org/10.1007/s11356-019-07193-5

10. Zheng, C., Yang, H., Cui, Z., Zhang, H., & Wang, X. (2017). A novel $Bi_4Ti_3O_{12}$/Ag3PO4 heterojunction photocatalyst with enhanced photocatalytic performance. *Nanoscale Research Letters*, 12, article 608.
https://doi.org/10.1186/s11671-017-2377-1

11. Banerjee, A. M. (2012). Thesis: Synthesis, characterization and catalytic activity of novel mixed oxides for energy and environmental related reactions. *Homi Bhabha National Institute.*
http://shodhganga.inflibnet.ac.in/handle/10603/11595

12. Shi, H., Tan, H., Zhu, W.-B., Sun, Z., Ma, Y., & Wang, E. (2015). Electrospun Cr-doped $Bi_4Ti_3O_{12}$/$Bi_2Ti_2O_7$ heterostructure fibers with enhanced visible-light photocatalytic properties. *Journal of Materials Chemistry* A, 12, 6586-6591.
https://doi.org/10.1039/C4TA06736C

13. Zhang, Y., Gao, J., Chen, Z., & Lu, Z. (2018). Enhanced photocatalytic performance of $Bi_4Ti_3O_{12}$ nanosheets synthesized by a self-catalyzed fast reaction process. *Ceramics International*, 44(18), 23014-23023.
https://doi.org/10.1016/j.ceramint.2018.09.103

14. McInnes, A., Sagu, J. S., & Wijayantha, K. G. U. (2014). Fabrication and photoelectrochemical studies of $Bi_2Ti_2O_7$ pyrochlore thin films by aerosol assisted chemical vapour deposition. *Materials Letters*,137, 214-217.
https://doi.org/10.1016/j.ceramint.2018.09.103

15. Akihiko, K., & Satoshi, H. (1999). H_2 or O_2 evolution from aqueous solutions on layered oxide photocatalysts consisting of Bi^{3+} with $6s^2$ configuration and d^0 transition metal ions. *Chemistry Letters*, 28(10), 1103-1104.
https://doi.org/10.1246/cl.1999.1103

16. Yao, W. F., Xu, X. H., Wang, H., Zhou, J. T., Yang, Z. N., Zhang, Y. *et al.* (2004). Photocatalytic property of perovskite bismuth titanate. *Applied Catalysis B: Environmental*, 52(2), 109-116.
https://doi.org/10.1016/j.apcatb.2004.04.002

17. Liu, Z., An, Y., Zhang, W., Zhu, L., & Zhu, G. (2023). Au Nanoparticles Modified Oxygen-vacancies-rich $Bi_4Ti_3O_{12}$ Heterojunction for Efficient Photocatalytic NO Removal with High Selectivity. *Journal of Alloys and Compounds*, 942, 169018.
https://doi.org/10.1016/j.jallcom.2023.169018

18. Zhao, Y., Fan, H., Fu, K., Ma, L., Li, M., & Fang, J. (2016). Intrinsic electric field assisted polymeric graphitic carbon nitride coupled with $Bi_4Ti_3O_{12}$/$Bi_2Ti_2O_7$ heterostructure nanofibers toward enhanced photocatalytic hydrogen evolution. *International Journal of Hydrogen Energy*, 41(38), 16913-16926.
https://doi.org/10.1016/j.ijhydene.2016.07.162

19. Morad, I., Alshehri, A. M.M Mansour, A. F., Wasfy, M. H., & El-Desoky, M. M. (2020). Facile synthesis and comparative study for the optical performance of different TiO_2 phases doped PVA nanocomposite films. *Physica B: Condensed Matter*, 597, 412415. https://doi.org/10.1016/j.physb.2020.412415

20. Hou, J., Yang, C., Wang, Z., Zhou, W., Jiao, S., & Zhu, H. (2013). In situ synthesis of α–β phase heterojunction on Bi_2O_3 nanowires with exceptional visible-light photocatalytic performance. *Applied Catalysis B: Environmental*, 142-143, 504-511. https://doi.org/10.1016/j.apcatb.2013.05.050

21. Anu, & Yadav, K. (2020). Optical and dielectric properties of $Bi_2Ti_2O_7/Bi_4Ti_3O_{12}$ nano-composite. *MaterialsToday: Proccedings*, 28(1), 153-157. https://doi.org/10.1016/j.matpr.2020.01.467

22. Ho, C.-H., Chan, C.-H., Huang, Y.-S., Tien, L.-C., & Chao, L.-C. (2013). The study of optical band edge property of bismuth oxide nanowires α-Bi_2O_3. *Optics Express*, 21(10), 11965-11972. https://doi.org/10.1364/OE.21.011965

23. Challagulla, S., Tarafder, K., Ganesan, R., & Roy, S. (2017). Structure sensitive photocatalytic reduction of nitroarenes over TiO_2. *Scientific Reports*, 7, article 8783. https://doi.org/10.1038/s41598-017-08599-2

24. Turner, C., Johns, P. M., Thatcher, E. M., Tanner, D. B., & Nino, J. C. (2014). Atomic displacive disorder in $Bi_2Ti_2O_7$. *Journal of Physical Chemistry C*, 118(49), 28797-28803. https://doi.org/10.1021/jp5095883

25. Makula, P., Pacia, M., & Macyk, W. (2018). How to Correctly Determine the Band Gap Energy of Modified Semiconductor Photocatalysts Based on UV-Vis Spectra. *Journal of Physical Chemistry Letters*, 9(23), 6814-6817. https://doi.org/10.1021/acs.jpclett.8b02892

26. Liu, Z., An, Y., Zhang, W., Zhu, L., & Zhu, G. (2023). Au Nanoparticles Modified Oxygen-vacancies-rich $Bi_4Ti_3O_{12}$ Heterojunction for Efficient Photocatalytic NO Removal with High Selectivity. *Journal of Alloys and Compounds*, 942, 169018. https://doi.org/10.1016/j.jallcom.2023.169018

27. Nogueira, A. E., Longo, E., Leite, E. R., & Camargo, E. R. (2014). Synthesis and photocatalytic properties of bismuth titanate with different structures via oxidant peroxo method (OPM). *Journal of Colloid and Interface Science*, 415, 89-94. https://doi.org/10.1016/j.jcis.2013.10.010